Zero-thermal-hysteresis Magnetocaloric Effect Induced by Magnetic Transition at Morphotropic Phase Boundary in Heusler Ni50Mn36Sb14-xInx Alloys

Journal:	*Physical Chemistry Chemical Physics*
Manuscript ID	CP-ART-04-2018-002720.R1
Article Type:	Paper
Date Submitted by the Author:	02-Jun-2018

Complete List of Authors:	zhang, yin; Xi'an Jiaotong University, School of Science Wang, Jieqiong; Hainan University Ke, Xiaoqin; Xi'an Jiaotong University Chang, Tieyan; Xi'an Jiaotong University, School of Science Tian, Fanghua; xi'an jiaotong university, Zhou, Chao; Xi\'an Jiaotong University, Department of Physics Yang, Sen; Xi'an Jiaotong University, School of Science Fang, Minxia; xi'an jiaotong university, Multi-Disciplinary Materials Research Center, Frontier Institute of Science and Technology, and State Key Laboratory for Mechanical Behavior of Materials Cao, Kaiyan; Xi'an Jiaotong University Chen, Yu-Sheng; University of Chicago Advanced Photon Source,, ChemMatCARS Sun, Zhanbo; Xi'an Jiaotong University, Physics Guan, Wen; Xi'an Jiaotong University Song, Xiaoping; Xi\'an Jiaotong University, Department of Physics Ren, Xiaobing; Xi\'an Jiaotong University

Physical Chemistry Chemical Physics

ARTICLE

Zero-thermal-hysteresis Magnetocaloric Effect Induced by Magnetic Transition at Morphotropic Phase Boundary in Heusler $Ni_{50}Mn_{36}Sb_{14-x}In_x$ Alloys

Received 00th January 20xx,
Accepted 00th January 20xx

DOI: 10.1039/x0xx00000x

www.rsc.org/

Yin Zhang, [a] Jieqiong Wang,[b] Xiaoqin Ke,[c] Tieyan Chang,[a,d] Fanghua Tian,[a] Chao Zhou, [a] Sen Yang, [a, †] Minxia Fang,[c] Kaiyan Cao,[a] Yu-Sheng Chen,[d] Zhanbo Sun,[a] Wen Guan,[a] Xiaoping Song,[a] and Xiaobin Ren [c]

With the development of magnetic refrigerant technology, the magnetic substances owning large magnetocaloric effect (MCE) with nearly zero thermal hysteresis are desired. Although Ni-Mn based Heusler alloys have been found to produce large MCE and attracted increasing attention recently, the occurrence of thermal hysteresis accompanying MCE due to the nature of first-order phase transition limits its application in the magnetic refrigeration. Up to now, an effective theory or method to eliminate this thermal hysteresis is still lacking. Here we propose to utilize the feature of magnetic transition at morphotropic phase boundary (MPB) to eliminate the thermal hysteresis and thus design a MPB-involved phase diagram in Heusler alloys of $Ni_{50}Mn_{36}Sb_{14-x}In_x$ (x=0-14). As theoretically expected, the magnetic transition at MPB really yields a MCE with a negligible thermal hysteresis (~ 0K) and the refrigerant capacity arrives at a maximum value of 108.2 J kg^{-1} at the composition of x=9. Our findings provide an effective way to design the large MCE materials with zero thermal hysteresis.

1 Introduction

Magnetocaloric effect (MCE) is a magneto-thermodynamic phenomenon occurring in magnetic materials; it is often manifested as an adiabatic temperature change or isothermal entropy variation induced by external magnetic field. Based on this MCE, magnetic refrigeration is being developed to be an environmentally friendly refrigeration technology with high efficiency and therefore has gained strong scientific interests. [1,2] Generally speaking, MCE is an intrinsic property of all magnetic substances but being particularly pronounced in the vicinity of transition temperature *Tc* of magnetic first-order transition, where magnetization sharply changes with temperature and external field.[3,4] For these materials, such as $Gd_5Ge_2Si_2$,[5] $LaFe_{11.7}Si_{1.3}$,[6] $MnAs_{1-x}Sb_x$,[7] $Ni_{50}Mn_{50-x}Sn_x$,[8] etc., a magnetic first-order transition from paramagnetic or antiferromagnetic state to ferromagnetic state yields a significant giant MCE under an external field. However, high refrigeration efficiency also relies on the reversibility of magnetizing and demagnetizing the refrigerant; such reversibility is far from guaranteed due to the nature of first-order transition. Since there is an energy barrier between high-temperature phase and low-temperature phase at Curie temperature (T_C) during first-order transition, a large thermal hysteresis must be induced by supercooling and superheating to run a refrigerating cycle, leading to lower refrigeration efficiency. It was reported that the thermal hysteresis dissipated most of the energy during cycling refrigeration work, and only ~5% of the corresponding entropy change (ΔS) could contribute to magnetic refrigeration prototype.[9] Finding an approach to eliminate (or reduce) the thermal hysteresis and simultaneously retain the large refrigerant capacity becomes urgent before this magnetic refrigeration can be widely put into service. Although several methods have been successfully employed to eliminate the thermal hysteresis (by doping foreigner elements or changing annealing conditions),[10,11] an effective theory and its corresponding method are still lacking.

Recently, the morphotropic phase boundary (MPB) has attracted significant interests in both ferroelectrics and ferromagnets owing to its contribution to designing materials with both highly responsive properties (e.g. large piezoelectricity and magnetostriction) and small thermal hysteresis.[12,13] This is due to the feature of phase transition at MPB. To well describe this feature, we use the sixth order Landau polynomial to calculate energy potential as follows:[14]

$$= f_0 + Am^2 + Bm^4 + Cm^6 + B'(m_1^2m_2^2 + m_2^2m_3^2 + m_1^2m_3^2) + C'm_1^2m_2^2m_3^2 \quad (1)$$

[a] MOE Key Laboratory for Non-Equilibrium Synthesis and Modulation of Condensed Matter State Key Laboratory for Mechanical Behavior of Materials, Xi'an Jiaotong University, Xi'an 710049, P.R.China
[b] State Key Laboratory of Marine Resource Utilization in South China Sea College of Materials and Chemical Engineering, Hainan University, Haikou 570228, P. R. China
[c] Frontier Institute of Science and Technology, Xi'an Jiaotong University, Xi'an 710049, P.R. China
[d] ChemMatCARS, The University of Chicago, Advance Photon Source, Argonne, Illinois 60439, United States
† corresponding to Sen Yang, email address: yang.sen@xjtu.edu.cn

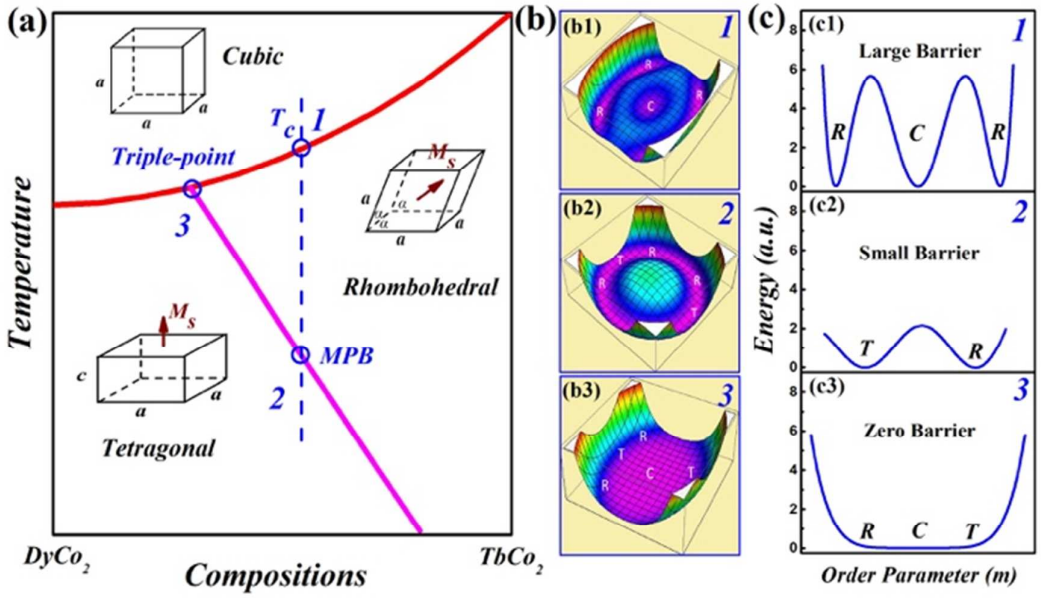

Fig. 1 Feature of magnetic transitions in MPB-involved phase diagram: (a) MPB-involved phase diagram mimicking our previously reported $Tb_{1-x}Dy_xCo_2$ system. (b) Calculated landscape of energy potential at T_C, MPB and triple point, which are marked as 1, 2 and 3 in Fig. 1(a). (c) Energy versus order parameter (magnetization) demonstrating the transition barrier of magnetic transitions at *Tc*, MPB and triple point.

where f_0 is the free energy of paramagnetic phase, m is the order parameter of magnetization vector, m_i is the component of magnetization along the x_i direction, and *A, B, B', C* and *C'* are Landau coefficients linked to temperature and composition. By choosing appropriate coefficients, a phase diagram mimicking our previously reported MPB-involved phase diagram in $Tb_{1-x}Dy_xCo_2$ system can be drawn in the Fig. 1a.[15] The landau parameters used in equation (1) are adjusted as follows: $A=4.124\times10^{-3}\times$ (T-55-50c), $B=-4\times|c-0.3|$, C=12.94, $B'=-(c-0.3)-0.003\times(T-70)$, $C'=-4\times(c-0.3)$, where c is the composition and T is the temperature. Such parameters were chosen to produce a phase diagram similar to that of Tb1-xDyxCo2 system and the calculation performed here can only be regarded as a qualitative analysis rather than a quantitative one. As seen, it is a typical MPB-involved phase diagram, where the T_C line and MPB line converge to a triple point of coexistence of cubic (C), tetragonal (T) and rhombohedral (R) phases, and the corresponding landscape of energy potential at T_C, MPB and triple point are depicted respectively in the Fig. 1b1, 1b2 and 1b3. Compared with the magnetic transition at T_C, a magnetic transition at MPB demonstrates a flat potential well and hence the R and T phases can be switched to each other easily. As a result, the highly responsive properties (e.g. magnetostriction) can be easily triggered by a small magnetic field at the MPB composition. Meanwhile, it is interesting to note that the transition barrier between high-temperature phase and low-temperature phase is much lower than that of magnetic transition at T_C and furthermore gradually decrease to zero at the triple point, as shown in Fig. 1c1, 1c2 and 1c3. This implies that the magnetic transition at MPB is a second-order transition (or weakly first-order transition) and thus exhibits zero (or small) thermal hysteresis. Based on the above analysis, we propose to utilize the feature of magnetic transition at MPB to design MCE materials to possess both large refrigerant capacity and nearly zero thermal hysteresis.

Among a large number of MCE materials, Heusler alloys are the ideal candidates for designing a MPB-involved phase diagram due to their rich physics of phase transitions coupled to the magnetization and crystal structure;[16,17] thus the diversity of their magnetic transitions can be easily controlled by tuning chemical compositions.[18,19] Recently, it has been reported that Heusler alloys of $Ni_{50}Mn_{50-x}In_x$ and $Ni_{50}Mn_{50-y}Sb_y$ will undergo a magnetically martensitic transition (MMT) at the range of x<16.5 and y<15.5, respectively.[18,20] Interestingly, these two MMTs share the same parent phase with cubic $L2_1$ crystal structure at high temperature, but showing different crystal structures and magnetic properties in martensitic state at low temperature. This situation about phase transitions in Heusler alloys is analogous to our understanding of MPB, and thus we designed a magnetic MPB-involved phase diagram in Heusler alloys of $Ni_{50}Mn_{36}Sb_{14-x}In_x$ (x=0-14). As expected, the magnetic transition at MPB really yields a MCE with a negligible thermal hysteresis (~0 K) and furthermore the refrigerant capacity (RC) achieve maximum value of 108.2 JKg^{-1} with a wider working temperature range at the composition of x=9. These results provide an effective way leading to large MCE materials with zero thermal hysteresis.

2 Results and discussion

2.1 Temperature Dependence of Magnetization and Heat Flow

Fig. 2 depict the magnetization curves as a function of temperature *M-T* and DSC of different compositions, providing

structural and magnetic phase transitions details. Herein, the *M-T* curves were measured under field cooling (FC) and zero field heating (FH) at low applied magnetic field (100 Oe) from 5 K to 400 K. The alloys contained various transitions, and as seen, each transition is significantly influenced by the compositions. The transition from paramagnetic to ferromagnetic first occurred at Curie temperature in austenitic state (T_c^A=331K) for the sample x=0. As temperature further decreased, a sudden drop in magnetization was observed, where the sample underwent a magnetic martensitic transformation (MMT) at 250K. Accordingly, two exothermic and endothermic peaks appeared during the cooling and heating processes in the corresponding DSC curves. The presence of a distinct hysteresis between the FC and FH is a strong evidence of first order transition, consistent with the observed thermal hysteresis (~20 k) in DSC. The MT can be observed in all the present compositions, however, the martensite start temperature (T_{Ms}) and austenite finish temperature (T_{Af}) moved upward as In substitution rose, coinciding with the calorimetry peak.

Interestingly, a new magnetic transition absent in previous compositions was appeared from the alloys with x=5, named Curie temperature in martensite state (T_c^M), During transition, the magnetization kept increasing as temperature decreased to below T_c^A, possibly related to another magnetic transition from a weak magnetic state to ferromagnetic state. With further increasing In content, a spin glass state begins to appear, which can be verified by two typical characters of spin glass (i.e., deviation between zero field cooling (ZFC) and FC curves, and the frequency dependence of ac susceptibility below the glass transition temperature T_g); for instance, such two characters of spin glass are demonstrated at the composition of x=14 as shown in the Fig. 2c. The emergence of spin glass can be ascribed to the presence of competitions between antiferromagnetic state and ferromagnetic state.

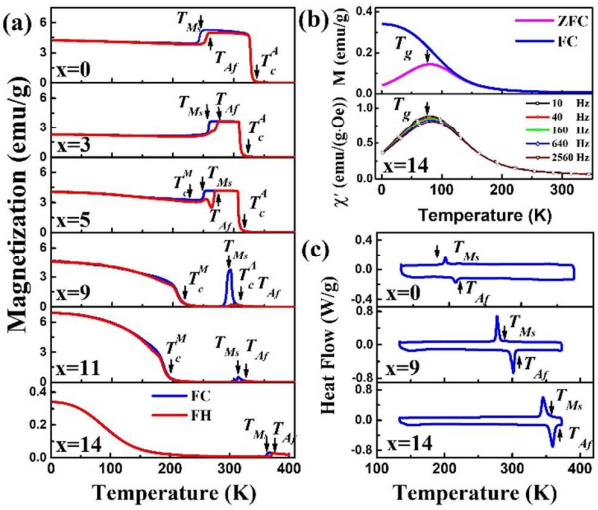

Fig. 2 (a) Temperature dependence of magnetization under FC and FH processes measured in presence of 100 Oe external magnetic field of selected compositions. (b) Temperature dependence of magnetization under ZFC and FC processes measured in presence of 100 Oe external field as well as the temperature dependence of *ac* susceptibility measured at 10 Oe ac field with different frequencies for the sample with composition of x=14. (c) DSC measurement during cooling and heating processes at the rate of 10 K/min of selected compositions.

2.2 Crystal symmetry and evolution

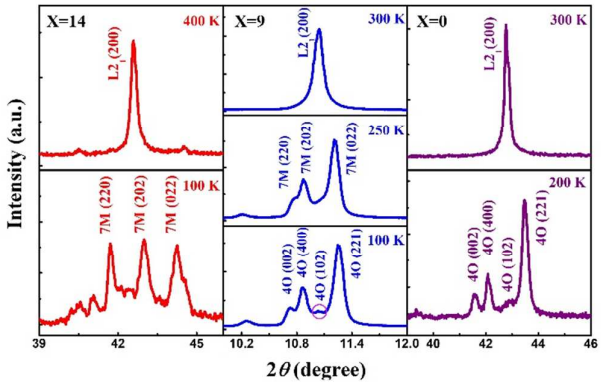

Fig. 3 *The* XRD spectra of $Ni_{50}Mn_{36}Sb_{14-x}In_x$ alloys with composition of x=14, x=9, and x=0 at different temperatures .

To determine the crystal symmetry of all phases, XRD spectra were conducted to observe the temperature dependent structure change in Fig. 3. As seen, the alloys of x=14 and x=0 both exhibit the same $L2_1$ cubic crystal structure in austenitic state at $T>T_{Ms}$. However, they display different crystal structure in martensitic state at lower temperature: the sample of *x*=0 demonstrates a modulated four-layered orthorhombic structure (4O) and the samples of *x*=14 display a modulated seven-layered monoclinic structure (7M), which are well agreed with previous reports.[19,21-23] Thus, it is expected to trace a transition from 7M to 4O in these compositions. From the *M-T* curves, the T_c^M associated a magnetic transition appeared at the composition from x=5 to x=9 is then considered.

Due to the small crystal symmetry difference, high-resolution synchrotron X-ray diffraction experiments (beamline ChemmatCARS, 15-ID-D, Advanced Photon Source (APS),

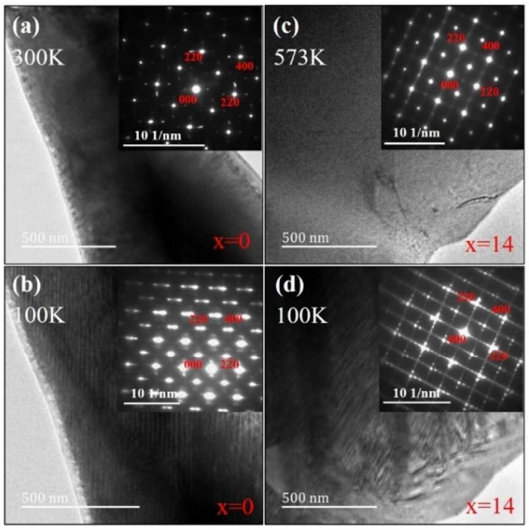

Fig.4 Temperature dependence of TEM micrograph and selected area electron diffraction patterns (SAED) of selected compositions at x=0 and x=14. a) For x=0 at T=300 K). b) For x=0 at T=100 K). c) For x=14 at T=573 K). d) For x=14 at *T*=100 K .

Argonne National Laboratory) were performed particularly. As

expected, it is well indexed as $L2_1$ austenitic phase with cubic structure at 300K in the x=9 alloy. When temperature decreases to 250K ($T_{Ms}>T>T_c^M$), the XRD profiles are clearly indicated as 7M modulated martensitic structure due to the disappearance of $L2_1(200)$ reflection anappearance of three characteristic 7M reflections. With further lowering temperature to 100K ($<T_c^M$), the XRD profiles can be denoted as 4O modulated martensitic structure due to the appearance of 4O (102) reflection. Further, transmission electron microscope (TEM) was applied to observe the temperature dependent structure change. Fig. 4 exhibits TEM microstructure with temperature change of selected samples at the composition of x=0 and x=14. As seen in Fig. 4a and 4c, both samples exhibit the same $L2_1$ cubic crystal structure in austenitic state at $T < T_{Ms}$, and with temperature decreasing to $T < T_{Ms}$, both samples undergo a martensitic transition from austenite to martensite and therefore manifest the martensitic variants structure (i.e., ferroelastic domains) as shown in Fig. 4b and 4d. The crystal structure evolution above is one prominent signature of MPB-involved phase diagram.

2.3 Phase diagram

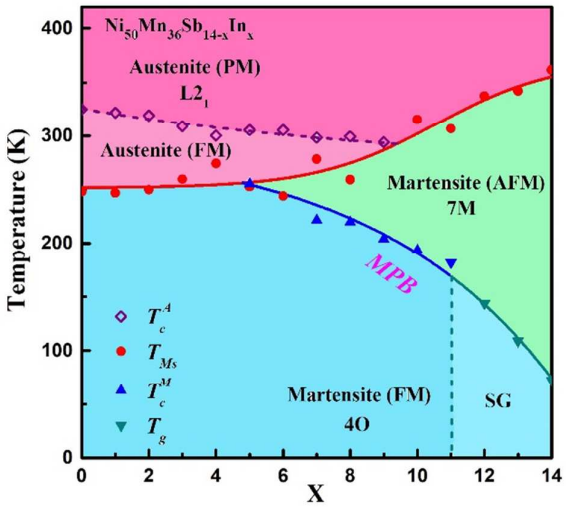

Fig. 5 MPB-involved phase diagram in Heusler alloys of $Ni_{50}Mn_{36}Sb_{14-x}In_x$ (x=0-14).

Fig. 5 shows our results of designed magnetic phase diagram in Heusler $Ni_{50}Mn_{36}Sb_{14-x}In_x$ (x=0-14) alloys and their corresponding measurement of transition temperature. As seen, it is a typical MPB-involved phase diagram and the two lines of phase transitions, one is a magnetically martensitic transition (MMT) from high-temperature austenite to low-temperature martensite and the other is a ferromagnetic transition in martensitic state (FTMS) from antiferromagnetic phase to ferromagnetic phase, intersect at the triple point at the composition of x=5. The transition temperatures (i.e., start temperature T_{Ms} of MMT, and Curie temperature T_c^M of FTMS) were determined by the measurement of temperature dependent magnetization (M-T curve) as shown in the Fig. 2a.

It is seen that the T_{Ms} is increased with the increase of In content in all the composition from x=0 to x=14; on the contrary, the T_c^M starts from the triple point at x=5 and then it is decreased with the increase of In content until x=11. As a result, a MPB line in the Fig. 5 is composed of transition temperatures of T_c^M and T_g. It is interesting to note, whether the transition at MPB is a FTMS or a spin glass transition, no thermal hysteresis (or small thermal hysteresis) occurs in the M-T measurement during the FC/FH cycle (see the Fig. 2a) due to the nature of a second-order (or weakly first-order) transition as we described in Fig. 5. Compared with the transition at MPB, the MMT at T_{Ms} is a typically first-order transition, accompanied by the exothermic and endothermic peaks as well as a large thermal hysteresis during cooling and heating process as shown in the DSC measurement (Fig. 2c). Obviously, this indicates that the magnetic refrigeration caused by a MMT will inevitably bring out the thermal hysteresis; by contrast, the magnetic refrigeration will produce nearly zero thermal hysteresis if it is driven by the magnetic transition at MPB.

Apparently, the MPB line is a phase boundary to separate the 4O and 7M structure and one endpoint of MPB line intersects with T_{Ms} line to form the triple point. From the MPB-involved phase diagram, it can be concluded that two different magnetic states varying compositions is the precondition of constructing MPB, and the small crystal structure difference is another prominent signature factor. The crystal structure change at MPB reveals the strong coupling of magnetization and crystal structure, which further indicates that a large MCE can be induced by the magnetic transition at MPB.

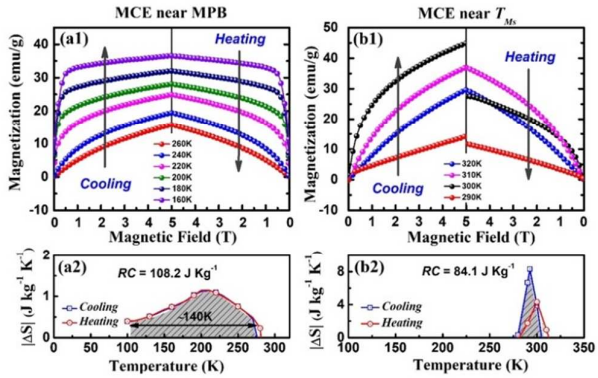

Fig. 6 Magnetocaloric effect near MPB and T_{M_s} of selected sample with composition at x=9. (a1) Isothermal magnetization curves at different temperatures during cooling and heating processes near MPB. (a2) Magnetic entropy change ΔS versus temperature under 5 Tesla during cooling and heating processes near MPB. (b1) Isothermal magnetization curves at different temperatures during cooling and heating processes near T_{M_s}. (b2) Magnetic entropy change ΔS versus temperature under 5 Tesla during cooling and heating processes near T_{M_s}.

2.4 Magnetocaloric effect

Fig. 6 illustrates the magnetocaloric effect (MCE) both at MPB and T_{Ms} of selected sample with composition at x=9. As described above, this sample undergoes a magnetically martensitic transition (MMT) at T_{Ms} and a ferromagnetic transition in martensitic state (FTMS) at MPB in turn with temperature decreasing from the high-temperature austenitic state. To evaluate the effect of thermal hysteresis on the MCE

of these two magnetic transitions, the isothermal magnetization (*M-H*) curves during cooling and heating processes in the vicinity of T_c^M and T_{Ms} are shown in Fig. 6a1 and 6b1, respectively. It is clearly seen that these two magnetic transitions exhibit different magnetization behaviour during cooling and heating processes: the *M-H* curves coincide well with each other for a FTMS at MPB (Fig. 6a1) but have tremendous mismatch for a MMT at T_{Ms} (Fig. 6b1). According to these *M-H* curves, the temperature dependent magnetic entropy change ΔS during cooling and heating processes can be estimated by using the Maxwell relationship and are correspondingly plotted in Figure 6a2 and 6b2, respectively. It is noted that the ΔS values at MPB during cooling and heating processes overlap mutually (Fig. 6a2); this is obviously due to the second-order (or weak first-order) nature of magnetic transition occurring at MPB and thus there is almost no thermal hysteresis accompanying the FTMS. On the contrary, an irreversible ΔS curves at T_{Ms} are obtained during cooling and heating processes (Fig. 6b2), which is attributed to the first-order nature of MMT at T_{Ms} and hence there exists a large thermal hysteresis in refrigeration cycle to reduce the refrigerant efficiency.

As a figure-of-merit of refrigeration, the refrigerant capacity (RC) is used to evaluate the magnetocaloric effect, referring to a measurement of heat transport between hot and cold reservoirs in an ideal refrigeration cycle. Generally, the RC value can be calculated by the following equation:

$$RC = \int_{T_1}^{T_2} \Delta S_H(T) dT \qquad (2)$$

where T_1 and T_2 are the temperatures of the cold and hot reservoirs in refrigeration cycle, respectively. Although the maximum value of Δ*S* (~1.2 $Jkg^{-1}K^{-1}$) at MPB of selected sample with composition at *x*=9 is smaller than that of MMT at T_{Ms} , its refrigerant temperature range (~140 K) is much wider than that of MMT and thus it may result in a large RC value. The shadow area under Δ*S* peaks in Fig. 6a2 and 6b2 respectively represents the RC value occurring at MPB and T_{Ms} . By calculating, the RC value at MPB can achieve 108.2 J kg^{-1}, which is much higher than that of MMT (~84.1 Jkg^{-1}). It is worth to note that such a RC value was strikingly higher than that of many other Ni-Mn based Heusler alloys, such as $Ni_{50}Mn_{38}Sb_{12}$ (40.5 Jkg^{-1}) and $Ni_{49.8}Co_{1.2}Mn_{33.5}In_{15.5}$ (76.6 Jkg^{-1}), and even comparable to $Ni_2Mn_{0.95}Cr_{0.05}In$ (153.91 Jkg^{-1}).[24-26] Surely, this result demonstrates that the large MCE with nearly zero thermal hysteresis can be induced by the magnetic transition at MPB, which can be more effectively used in magnetic refrigeration technology.

2.5 Discussion

To search for the maximum MCE occurring at MPB, we measure the MCE along the MPB line in Fig. 5 at the composition from *x*=5 to *x*=11 as shown in Table 1. It is seen that all the MCEs induced by FTMS at MPB were accompanied with zero thermal hysteresis; by contrast, the corresponding MCEs induced by MMT at T_{Ms} were accompanied with large thermal hysteresis. This is obviously due to the feature of magnetic transition at MPB as we described above. The maximum MCE at MPB occurs at the composition of *x*=9 and both Δ*S* and RC value simultaneously achieve the maximum. To our knowledge, however, the underlying physics of maximum MCE at *x*=9 is unclear, and it deserves to be further investigated. But, we note that there exists a ferromagnetic transition in austenitic state (FTAS) at T_c^A from paramagnetic phase to ferromagnetic phase, which is measured and drawn as a dash line in the Fig. 5. Such a FTAS is merged with T_c^M line into the triple point in the austenite just at the composition of *x*=9, resulting in a unique change of abrupt peak in the *M-T* curve as shown in Fig. 2a. This implies that the magnetization becomes extremely sensitive to the temperature and magnetic field; thus it may give rise to the large MCE at the composition of *x*=9. A detailed study is still in progress and will be reported elsewhere. In a word, the MPB-involved phase diagram with a unique triple-point provides a method to design the magnetic materials with largely MCE with zero thermal hysteresis.

Table 1 Comparison of the MCE performance near MPB and T_{M_s} during cooling and heating processes of selected compositions, including magnetic entropy change Δ*S*, refrigerant capacity RC, thermal hysteresis Δ*T*

$Ni_{50}Mn_{36}Sb_{14-x}In_x$	MCE near MPB			MCE near T_{M_s}		
	$\lvert\Delta S\rvert$ ($J\,Kg^{-1}K^{-1}$)	*RC* ($J\,Kg^{-1}$)	Δ*T* (K)	$\lvert\Delta S\rvert$ ($J\,Kg^{-1}K^{-1}$)	*RC* ($J\,Kg^{-1}$)	Δ*T* (K)
x=5	0.2	7.9	~0	4.5	40.6	10.7
x=7	0.8	49.7	~0	4.7	44.7	9.4
x=9	1.2	108.2	~0	8.3	84.1	7.4
x=11	0.7	31.3	~0	1.4	13.4	2.0

3 Conclusions

In summary, we design a MPB-involved phase diagram in Heusler alloys $Ni_{50}Mn_{36}Sb_{14-x}In_x$ (x=0-14) and report a large MCE with nearly zero thermal hysteresis induced by magnetic transition at MPB. Such a MCE at MPB is caused by a second-order (or a weak first-order) FTMS from an antiferromagnetic phase to a ferromagnetic phase. The maximum RC value occurs at the composition of x=9 and can achieve 108.2 J kg^{-1}, which is much higher than that of first-order MMT in the same alloy. Obviously, our results provide a method to utilize the feature of MPB-involved phase diagram to fabricate the magnetic materials with largely zero-thermal-hysteresis magnetocaloric effect and thus promote their potential application in the refrigerator technology.

4 Experimental

The ingots of $Ni_{50}Mn_{36}Sb_{14-x}In_x$ (x=0-14) alloys were prepared by arc melting of high-purity Ni (99.9%), Mn (99.9%), Sb (99.9%) and In (99.9%) in argon atmosphere. To ensure the composition homogeneity, all the ingots were melted many times and the weight loss was less than 0.5%. After melting, all the samples were sealed into the silica tubes in vacuum and then were annealed at 1173 K for 24 hours for further composition homogeneity. The measurements of magnetic properties, including magnetic hysteresis loops, magnetization-temperature (*M-T*) curve and ac susceptibility were carried out by the superconducting quantum interference device (SQUID). To check the thermal hysteresis, the *M-T* curves were measured both under the field-cooling (FC) process and field-heating (FH) process by applying 100 Oe external field. To determine the spin glass transition at the samples with the composition from x=12 to x=14, the M-T curves were also measured both under the zero-field-cooling (ZFC) process and field-cooling (FC) process. The Differential scanning calorimetry (DSC) was used to check the first-order transitions. The X-ray diffraction (XRD) measurements were performed on a Bruker D8 X-ray diffractometer using Cu-Kα radiation with λ=1.5406 Å. To detect the unremarkable structure change of x=9, we measured this sample using the synchrotron radiation with λ=0.41328 Å (beamline ChemmatCARS, 15-ID-D, Advanced Photon Source (APS), Argonne National Laboratory). The structural changes of magnetic transitions in MPB-involved phase diagram were observed by transmission electron microscope (TEM, JEOL JEM-2100). To study the MCE behaviour, the magnetic entropy change of ΔS were estimated from M-H isotherms by using Maxwell relationship:

$$\Delta S(T,H) = \int_0^H (\frac{\partial M}{\partial T})_H \, dH \qquad (3)$$

from 0 to 5 Tesla. The refrigerant capacity (RC) was calculated by integrating the area under ΔS vs T curves, using the temperature range at half-maximum of the ΔS peak suggested by Gschneidner et al.[27]

Conflicts of interest

There are no conflicts to declare.

Acknowledgements

The acknowledgements come at the end of an article after the conclusions and before the notes and references. This work was supported by the National Natural Science Foundation of China (Grant No. 51701149, 51471125, 51601140, 51671155 and 51501142), Shaanxi Postdoctoral Science Foundation 2016BSHYDZZ10, the Fundamental Research Funds for the Central Universities (China) and Collaborative Innovation Center of Suzhou Nano Science and Technology. ChemMatCARS is principally supported by the Divisions of Chemistry (CHE) and Materials Research (DMR), National Science Foundation, under grant number NSF/CHE-1346572. Use of the PILATUS3 X CdTe 1M detector is supported by the National Science Foundation under the grant number NSF/DMR1531283

Notes and references

‡ Footnotes relating to the main text should appear here. These might include comments relevant to but not central to the matter under discussion, limited experimental and spectral data, and crystallographic data.

1 M. H. Phan, S. C. Yu, *J. Magn. Magn. Mater.* **2007**, 308, 325.
2 B. G. Shen, J. R. Sun, F. X. Hu, H. W. Zhang, Z. H. Cheng, *Adv. Mater.* **2009**, 21, 4545.
3 A. M. Tishin, *J. Magn. Magn. Mater.* **1998**, 184, 62.
4 F. Guillou, G. Porcari, H. Yibole, N. van Dijk, E. Bruck, *Adv. Mater.* **2014**, 26, 2671.
5 V. K. Pecharsky, J. K. A. Gschneidner, *Phys. Rev. Lett.* **1997**, 78, 4494.
6 F. X. Hu, M. Ilyn, A. M. Tishin, J. R. Sun, G. J. Wang, Y. F. Chen, F. Wang, Z. H. Cheng, B. G. Shen, *J. Appl. Phys.* **2003**, 93, 5503.
7 H. Wada, Y. Tanabe, *Appl. Phys. Lett.* **2001**, 79, 3302.
8 T. Krenke, E. Duman, M. Acet, E. F. Wassermann, X. Moya, L. Mañosa, A. Planes, *Nat. Mater.* **2005**, 4, 450.
9 P. J. Shamberger, F. S. Ohuchi, *Phys. Rev. B.* **2009**, 79, 144407.
10 H. Zhang, B. G. Shen, Z. Y. Xu, X. Q. Zheng, J. Shen, F. X. Hu, J. R. Sun, Y. Long, *J. Appl. Phys.* **2012**, 111, 07A909.
11 N. T. Trung, Z. Q. Ou, T. J. Gortenmulder, O. Tegus, K. H. J. Buschow, E. Bruck, *Appl. Phys. Lett.* **2009**, 94, 102513.
12 Z. Zhou, H. Tang, H. Sodano, *Adv. Mater.* **2014,** *26*, 7547
13 D. Hunter, W. Osborn, K. Wang, N. Kazantseva, J. H. Simpers; R. Suchoski, R. Takahashi, M. L.Young, A. Mehta, L. A. Bendersky, S. E. Lofland, M. Wuttig, *Nat. Commun.* **2011**, 2, 518.
14 P. C. Hohenberg, A. P. Krekhov, *Phys. Rep.* **2015**, 572, 1.
15 S. Yang, H. X. Bao, C. Zhou, Y. Wang, X. B. Ren, Y. Matsushita, Y. Katsuya, M. Tanaka, K. Kobayashi, X. P. Song, J. R. Gao, *Phys. Rev. Lett.* **2010**, 104, 197201.
16 T. Krenke, X. Moya, S. Aksoy, M. Acet, P. Entel, L. Mañosa, A. Planes, Y. Elerman, A. Yücel, E. F. Wassermann, *J. Magn. Magn. Mater.* **2007**, 310, 2788.
17 D. Y. Cong, S. Roth, L. Schultz, *Acta. Mater.* **2012**, 60, 5335.
18 T. Krenke, M. Acet, E. F. Wassermann, X. Moya, L. Mañosa, A. Planes, *Phys. Rev. B.* **2006**, 73, 174413.
19 F. H. Tian,Y. Y. Zeng, M. W. Xu, S. Yang, T. Lu, J. Q. Wang, T. Y. Chang, M. Adil, Y. Zhang, C. Zhou, X. P. Song, *Appl. Phys. Lett.* **2015**, 107, 012406.
20 Y. Sutoua, Y. Imano, N. Koeda, T. Omori, R. Kainumab, K. Ishida, *Appl. Phys. Lett.* **2004**, 85, 4358.
21 H. Seiner, V. Kopecký, M. Landa, O. Heczko, *Phys. Status. Solidi. B*. **2013**, 251, 2097.
22 Y. Wu, J. Wang, H. Hua, C. Jiang, H. Xu, *J. Alloy. Compd.* **2015**, 643, 681.
23 K. Fukushima, K. Sano, T. Kanomata, H. Nishihara, Y. Furutani, T. Shishido, W. Ito, R.Y. Umetsu, R. Kainuma, K. Oikawae, K. Ishida, *Scripta. Mater.* **2009**, 61, 813.
24 N. V. Nong, L. T. Tai, N. T. Huy, N. T. Trung, C. R. H. Bahl, R. Venkatesh, F. W. Poulsen, N. Pryds, *Mater. Sci. Eng. B-Adv.* **2011**, 176, 1322.
25 L. Huang, D. Y. Cong, L. Ma, Z. H. Nie, Z. L. Wang, H. L. Suo, Y. Ren, Y. D. Wang, *Appl. Phys. Lett.* **2016**, 108, 032405.
26 J. Brock, M. Khan, *J. Magn. Magn. Mater.* **2017**, 425, 1.

27 J. a. K. A. Gschneidner, V. K. Pecharsky, *Ann. Rev. Mater. Res.* **2000**, 30, 387.